Applied Catalysis O: Open 219 (2026) 207117

Contents lists available at ScienceDirect

Applied Catalysis O: Open

journal homepage: www.elsevier.com/locate/apcato

Effects of elemental substitution on catalytic properties of Tsai-type 1/1 quasicrystal approximants for acetylene hydrogenation

Haruka Yoshikawa [a,b,*,1], Ya Xu [a,*], Farid Labib [b], Satoshi Kameoka [c], Ryuji Tamura [b]

[a] Research Center for Energy and Environmental Materials, National Institute for Materials Science, 3-13 Sakura, Tsukuba, Ibaraki 305-0003, Japan
[b] Department of Materials Science and Technology, Tokyo University of Science, 6-3-1 Niijyuku, Katsushika, Tokyo 125-8585, Japan
[c] Institute of Multidisciplinary Research for Advanced Materials, Tohoku University, 2-1-1 Katahira, Aoba-ku, Sendai 980-8577, Japan

ARTICLE INFO

Keywords:
Acetylene hydrogenation
Quasicrystal approximant
Hard X-ray electron spectroscopy
Density functional theory
Catalytic activity
Non-equivalent crystallographic site
Adsorption energy

ABSTRACT

Quasicrystals (QCs) and their approximant crystals (ACs) have many nonequivalent sites that can be controlled by elemental substitution and composition variation of the alloy system. This structural control at the crystallographic site level enables the design of material functions. QCs and ACs are expected to be applied as catalysts, with their catalytic properties depending on the local surface structure. Previously, we reported the excellent catalytic properties of Al-Pd-Sc Tsai-type 1/1 AC. In this study, we systematically investigated the effects of elemental substitution in various ternary Tsai-type 1/1 ACs—(Al,Ga,In)-(Pd,Pt)-(Sc,Tb,Dy,Ho)—on their catalytic behavior in acetylene hydrogenation. Substituting Ga or In with Al most effectively enhanced catalytic activity, whereas substitution among rare-earth elements had only a minor influence. Among all examined compositions, Al–Pd–Sc exhibited the highest activity, and all ACs showed high ethylene selectivity (>90%). Hard X-ray photoelectron spectroscopy and density functional theory (DFT) calculations were employed to elucidate the origin of these effects. The Pd 3d binding energy in Al–Pd–Sc shifted to higher values upon replacing Ga with Al, indicating that the electronic state of Pd can be tuned through elemental substitution and compositional control. DFT analysis further revealed that three types of nonequivalent sites contribute significantly to the reaction. These findings demonstrate that both the electronic structure and geometric configuration of active sites in Tsai-type ACs can be modulated through elemental substitution, highlighting the potential of ACs as structurally designable catalysts.

1. Introduction

The catalytic properties of alloy materials are significantly affected by ligand effects, which arise from the electronic states of active atoms, as well as ensemble effects associated with the geometric structure surrounding these atoms, [1–5]. However, in conventional disordered alloy catalysts, these factors are difficult to control independently because the geometric and electronic structures cannot be precisely tuned. In recent years, intermetallic compounds with multiple nonequivalent crystallographic sites—particularly quasicrystals (QCs) and their approximant crystals (ACs)—have attracted considerable attention as promising platforms for designing high-performance catalysts. These materials follow the Hume–Rothery rule [6], stabilizing at an average number of valence electrons per atom (e/a) [7,8], and have been discovered in numerous alloy systems [9]. Both QCs and ACs exhibit a multi-shell atomic cluster structure, where atoms are arranged at the vertices of a polyhedron as a unit structure [8,10–23]. This unit structure is arranged quasiperiodically in QCs, whereas it is arranged periodically in ACs [9,24]. The structure of ACs is expressed in terms of fractions by symmetry. 1/1ACs have the symmetry of a body-centered cubic structure, and have been reported in many alloy systems.

Among these materials, Tsai-type QCs and ACs contain an icosahedral cluster in which rare-earth elements occupy the vertices of the inner icosahedral shell among various concentric shells (Fig. 1) [7,8,18]. This structural feature is expected to impart unique physical properties [25]. Several studies have explored the catalytic potential of QCs and ACs and demonstrated that specific active points are formed in their structures. Moreover, surface treatment can further enhance their catalytic activity

* Corresponding authors at: Research Center for Energy and Environmental Materials, National Institute for Materials Science, 3-13 Sakura, Tsukuba, Ibaraki 305-0003, Japan.
E-mail addresses: harukafrom.9@gmail.com (H. Yoshikawa), xu.ya@nims.go.jp (Y. Xu).
[1] Present affiliation: Mitsubishi Kakoki Kaisha, Ltd.

https://doi.org/10.1016/j.apcato.2026.207117
Received 5 March 2026; Received in revised form 3 September 2026; Accepted 11 September 2026
Available online 11 September 2026
2950-6484/© 2026 The Authors. Published by Elsevier B.V. This is an open access article under the CC BY license (http://creativecommons.org/licenses/by/4.0/).

by optimizing these active sites [26–32].

Acetylene (C_2H_2) hydrogenation is one of the simplest hydrogenation reactions, involving the addition of a hydrogen molecule to the triple bond between two carbon atoms. This reaction is crucial in organic synthesis because C_2H_2 poisons the catalyst when ethylene (C_2H_4) is used as the feedstock, and C_2H_2 hydrogenation is essential for removing C_2H_2 impurities from C_2H_4. Pd-based catalysts are widely used for this reaction because of their high activity [1]. However, their catalytic behavior is strongly influenced by ensemble effects [33,34], making it difficult to precisely control product selectivity [35]. In a recent study, we evaluated the catalytic properties of Al-Pd-Sc and Ga-Pd-Sc Tsai-type 1/1 ACs for C_2H_2 hydrogenation to achieve precise control of the catalytic performance by leveraging the non-equivalent crystallographic sites of ACs [36]. Al-Pd-Sc exhibited significantly higher catalytic activity than Ga-Pd-Sc, and both catalysts demonstrated high selectivity toward C_2H_4, with negligible formation of ethane. Density functional theory (DFT) calculations indicated that the adsorption energies of the reactants varied depending on the adsorption site, although only a subset of the adsorption sites was examined [36]. These findings suggest that substituting Ga with Al in Ga-Pd-Sc 1/1 AC, which contains eight non-equivalent sites, seven of which are occupied by Pd and Al or Ga [14,37], greatly enhances the catalytic activity. Since Ga and Al both belong to Group 13 of the Periodic Table, it is natural to ask whether other Group 13 elements (e.g., In) exhibit similar effects. It is also of interest to examine whether substitution at rare-earth sites (e.g., Tb, Dy, Ho → Sc) or active-metal sites (e.g., Pt → Pd) influences catalytic behavior in 1/1 ACs. Beyond electronegativity differences, previous XPS studies of Ni and Pd alloys have shown that d-band centroid shifts arise primarily from hybridization-induced redistribution of the d states and changes in bandwidth, rather than from simple charge transfer [38]. This suggests that the Pd 3d binding-energy shift observed upon Al/Ga substitution in Tsai-type 1/1 ACs likely reflects modifications of the Pd d-band structure caused by local coordination and orbital mixing.

This study aims to establish generalizable design principles for Tsai-type 1/1 AC catalysts by systematically investigating the effects of elemental substitution across Group 13 elements (Al, Ga, In), precious metals (Pd, Pt), and rare-earth elements (Sc, Tb, Dy, Ho) on the catalytic performance of Pd-containing ACs in C_2H_2 hydrogenation. Furthermore, because the reaction mechanism on Al–Pd–Sc and Ga–Pd–Sc surfaces was not fully elucidated in our previous work [36], we employed hard X-ray photoelectron spectroscopy (HAXPES) to analyze the electronic states of Pd, Al, and Ga in these ACs. Complementary DFT calculations were conducted to evaluate adsorption energies at different nonequivalent sites and to determine activation energies for elementary reaction steps occurring on Tsai-type 1/1 AC surfaces.

2. Experimental

2.1. Sample preparation

The compositions of various (Al,Ga,In)-(Pd,Pt)-(Sc,Tb,Dy,Ho) alloys used in this study are listed in Table 1. To ensure that each sample possessed a **single-phase 1/1 AC structure**, we selected these compositions that have been previously reported to form stable 1/1 ACs. Because Tsai-type ACs often exhibit narrow phase stability ranges, compositions with identical elemental ratios do not necessarily yield single-phase 1/1 ACs. The alloy ingots were prepared by arc melting under an Ar atmosphere using pure raw metals (>99.9% purity). X-ray diffraction (XRD) measurements (SmartLab SE, Rigaku) confirmed that all synthesized samples consisted almost entirely of a single-phase 1/1 AC phase (Fig. S1). Each sample for catalytic reaction was powdered in an Ar atmosphere using a mortar and sieved to less than 75 μm. The powder (0.1 g) was placed in a quartz tube for the reaction. The specific surface areas of the powder samples were measured using the Brunauer–Emmett–Teller (BET) method (ASAP 2020, Micrometrics) to confirm that all the samples exhibited comparable specific surface area (Table 1).

Table 1
Composition and specific surface area of prepared AC samples and references relating to the structure.

Composition (at. %)	Specific surface area (m^2/g)	Structure	Composition reference
$Al_{55}Pd_{30}Sc_{15}$	0.09	1/1 AC	[39]
$Ga_{55}Pd_{30}Sc_{15}$	0.11	1/1 AC	[16]
$Ga_{50}Pd_{36}Tb_{14}$	0.09	1/1 AC	[40]
$Ga_{50}Pd_{36}Dy_{14}$	0.20	1/1 AC	[12]
$Ga_{50}Pd_{36}Ho_{14}$	0.14	1/1 AC	[12]
$Ga_{51.5}Pt_{34}Tb_{14.5}$	0.08	1/1 AC	[10]
$In_{53}Pd_{33}Gd_{14}$	0.13	1/1 AC	[15]
$In_{53}Pd_{33}Tb_{14}$	0.12	1/1 AC	[15]

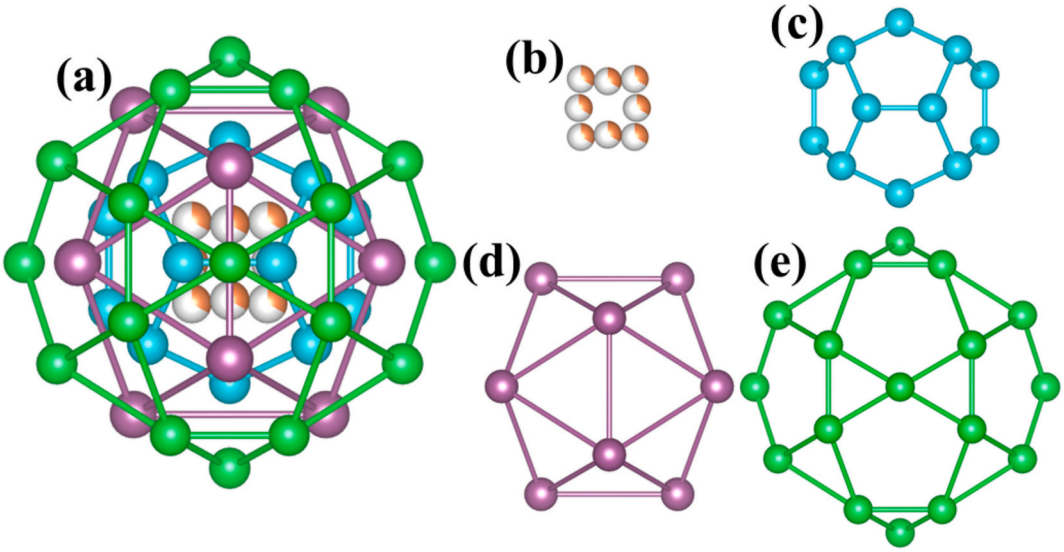


Fig. 1. Cluster structures of Tsai-type quasicrystals (QCs) and their approximant crystals (ACs). (a) Nested atomic clusters. (b) Central sites. (c) and (d) Icosahedral shells. (e) Icosidodecahedral shell [7,8,17].

2.2. Catalytic reaction

In our previous research [36], C_2H_2 hydrogenation catalytic reaction tests were conducted on Al-Pd-Sc and Ga-Pd-Sc systems in the temperature range of 60 to 200 °C. Their activity was highest at 200 °C. In this study, isothermal reaction tests were conducted at 200 °C to compare the catalytic activity of Tsai-type 1/1 ACs. The reaction tube containing the sample was attached to a fixed-bed flow reactor, and catalytic reaction tests were conducted at 200 °C for 5 h. The reaction gas compositions were C_2H_2: 0.5, H_2: 5.0, and N_2: 23.8 mL/min. The gas space velocity was 3.5×10^4 h^{-1}. Before the reaction, a hydrogen reduction treatment was performed on all samples under the N_2: 10 and H_2: 30 mL/min conditions. The gas composition after the reaction was analyzed using two gas chromatographs (GC323 and GC-4000 Plus, GL Sciences). H_2 and N_2 were measured using a thermal conductivity detector (TCD) and zeolite column, and C_2H_2, C_2H_4, and C_2H_6 were measured using a flame Ionization detector (FID) and a DVB-EVB-ethylene glycol dimethacrylate column (Porapak N 80/100, DVB: Divinylbenzene, EVB: Ethylvinylbenzene). The gas flow rate at the outlet was measured using a flowmeter (Definer 220, MesaLabs).

Selectivity of C_2H_4 ($S_{C_2H_4}$) was defined as the ratio of C_2H_4 formation to the total formation of C_2H_4 and C_2H_6.

$$R_{C_2H_2} = \frac{F_{C_2H_2,in} - F_{C_2H_2,out}}{\text{Surface area}}$$

$$S_{C_2H_4} = \frac{F_{C_2H_4,out}}{F_{C_2H_4,out} + F_{C_2H_6,out}} \times 100\%$$

where $R_{C_2H_2}$ is the reaction rate of C_2H_2 (mol min^{-1} m^{-2}), F_x is the flow rate of gas component x (mol min^{-1}), and the surface area is determined by BET measurements (m^2).

2.3. HAXPES analyses

HAXPES analyses were performed at the SPring-8 BL09XU beamline using synchrotron radiation with an incident energy of 7940 eV. To prevent oxidation, each alloy ingot was fractured inside a vacuum-sealed sample-exchange chamber and transferred into the measurement chamber without exposure to air. To examine the changes in the electronic state of Pd induced by elemental substitution in the Al-Pd-Sc and Ga-Pd-Sc systems, Pd 3d, Al 1 s, and Ga 2p spectra were collected the freshly fractured surfaces of the corresponding Tsai-type 1/1 ACs.

2.4. DFT calculations

DFT calculations were performed on the Al-Pd-Sc and Ga-Pd-Sc samples using PHASE/0 code [41]. The slab model contains 188 atoms, and its thickness corresponds to the lattice constant (~14 Å). The vacuum layer was set to 16 Å. Ultrasoft pseudopotentials were used for all atoms. The plane-wave cutoff energy was set to 450 eV, the charge density cutoff energy was set to 4050 eV, and Brillouin-zone sampling was performed using a $2 \times 2 \times 1$ k-point mesh. The electronic energy convergence criterion was set to 1×10^{-5} eV and the force criterion was set to 0.02 eV/Å.

Previous HAADF-STEM studies reported that Al-Pd-Sc and Ga-Pd-Sc do not exhibit well-defined stable surfaces [37]. Therefore, following our earlier work [36], we assumed that the (100), (110), and (111) planes coexist on the catalyst surface. In this study, we focused on the simplest (100) surface to clarify the influence of nonequivalent sites on catalytic properties.

Tsai-type 1/1 ACs structure consist of polyhedral atomic clusters located at each vertex of the unit cell. The rare-earth elements at the icosahedral sites are exposed on the surface of the Tsai-type 1/1 ACs [42]. Sc is exposed at two positions on the cross-section parallel to the surface (100): one passing through the center of the cluster and another passing through the edge of the icosahedron (Fig. 2). Because the former has a higher atomic surface density, slab models of Al–Pd–Sc and Ga–Pd–Sc were constructed with the (100) surface intersecting the cluster center. These ACs contain eight nonequivalent crystallographic sites: one icosahedral Sc site and seven sites (M1–M7) occupied by Pd and Al or Pd and Ga. Three of these seven sites exhibit partial occupancy by Pd/Al or Pd/Ga. The cluster-center site has an occupancy factor of 0.33 [14,37]. Since partially occupied sites cannot be directly represented in slab models, the element with the highest occupancy factor was assigned to each such site. The cluster center site formed a central unit with 12 equivalent positions in proximity; that is, the atoms were arranged to occupy four of these positions. Structural relaxation was performed with the top three atomic layers allowed to relax while the remaining layers were fixed. Fig. 3 shows the adsorption sites and surface crystallographic positions appearing on the slab, including M1, M2, M4, M5, M7, and Sc.

In our previous work, adsorption energies of C_2H_2 and C_2H_4 at Al—Pd bridge sites were reported [36]. In this study, we extended the calculations to include absorption at Sc—Pd, Sc—Al, and Sc sites, as well as the adsorption of $CHCH_2$. The adsorption energy ($E_{adsorption}$) was calculated using the following formula:

$$E_{adsorption} = E_{total} - E_{adsorbate} - E_{model}$$

where E_{total} is the total energy of the slab with the absorbed adsorbate, $E_{adsorbate}$ is the energy of the isolated adsorbate, and E_{model} is the energy of the clean slab. According to this definition, a low value of $E_{adsorption}$ corresponds to a strong adsorption.

Transition states for elementary reaction steps were determined using the climbing-image nudged elastic band (CI-NEB) method. Six intermediate images were used. To reduce computational cost, NEB models were constructed by removing atoms from the bottom half of the slab (Fig. 3). Initial and final states were taken from the relaxed adsorption structures. The transition state was defined as the highest-energy intermediate. Activation energies E_a and reaction enthalpies ΔH were calculated as:

$$E_a = E_{transition} - E_{initial}$$

$$\Delta H = E_{final} - E_{initial}$$

where $E_{transition}$, $E_{initial}$, and E_{final} are the total energies of the transition, initial, and final states, respectively.

3. Results and discussion

3.1. Catalytic reaction experiments

The reaction products consisted solely of C_2H_4 and trace amounts of C_2H_6. No hydrocarbons associated with C—C coupling or other side reactions were detected. Fig. 4 shows the catalytic activity and C_2H_4 selectivity of various Tsai-type 1/1 AC samples for C_2H_2 hydrogenation. The Al-Pd-Sc system exhibited the highest activity among the tested alloy systems. The C_2H_4 selectivity was greater than 90% for all samples. Samples with relatively low activity could not be clearly compared within this same graph; therefore, their individual reaction profiles are provided in Fig. S2.

Comparing Al–Pd–Sc and Ga–Pd–Sc, substitution of Ga with Al significantly increased catalytic activity. In contrast, replacing Ga with In in Ga–Pd–Tb and Ga–Pd–Gd (i.e., forming In–Pd–Tb and In–Pd–Gd) did not enhance activity. For Ga–Pt–Tb, where Pd in Ga–Pd–Tb was replaced with Pt, the catalytic activity increased upon elemental substitution. Although Pd is generally more active than Pt for C_2H_2 hydrogenation [1], the opposite trend was observed for the Tsai-type 1/1 ACs examined here.

For Ga–Pd–(Sc, Tb, Dy, Ho) systems, in which rare-earth elements occupy the icosahedral sites, Ga–Pd–Sc showed the highest activity.

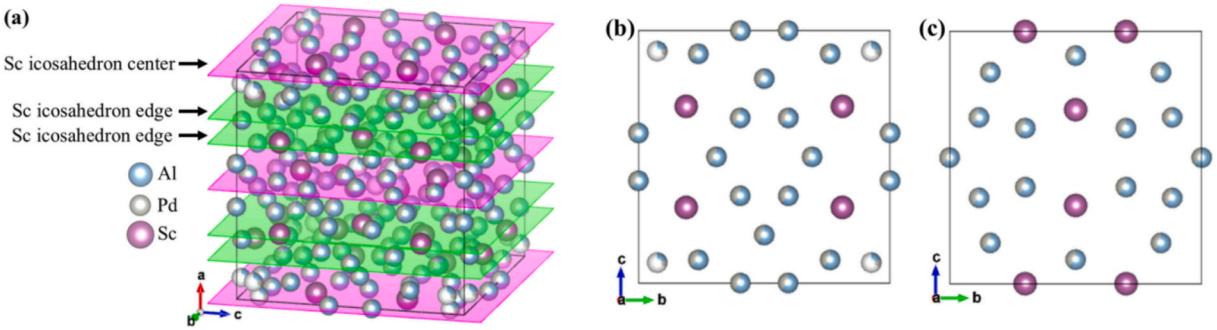


Fig. 2. (a) Two types of Al-Pd-Sc 1/1 AC (100) cross-sections. The cross-section passing through the center of the Sc 20 dodecahedron is shown in purple, and the cross-section passing through the edge is shown in green [36]. (b) Cross-section passing through the center of the Sc icosahedron. (c) Cross-section passing through the edge of the Sc icosahedron. (For interpretation of the references to colour in this figure legend, the reader is referred to the web version of this article.)

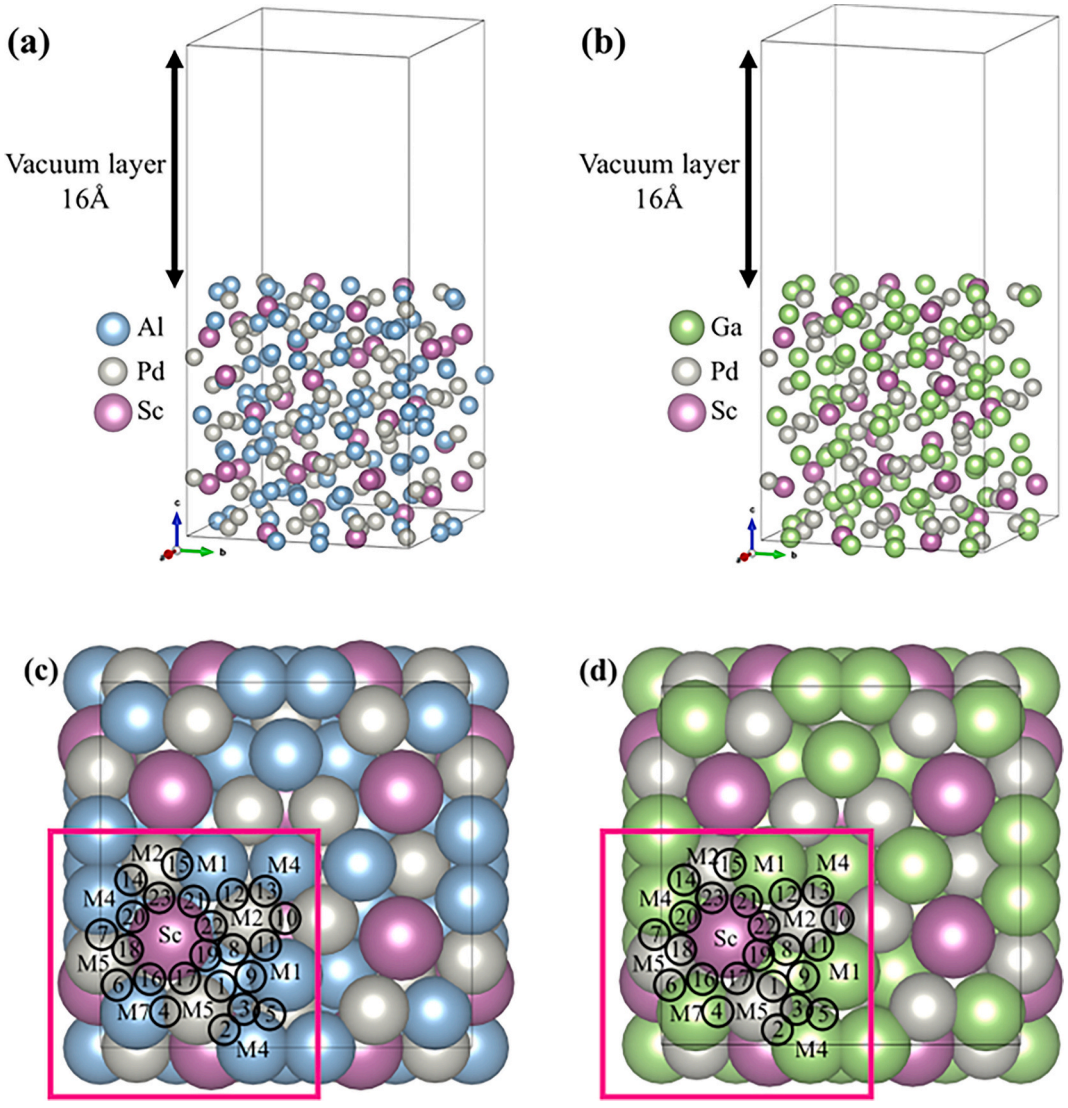


Fig. 3. Computational slab models of (a) Al–Pd–Sc 1/1 AC and (b) Ga–Pd–Sc 1/1 AC. Surface structures of (c) Al–Pd–Sc and (d) Ga–Pd–Sc viewed from the vacuum side. Bridge sites used for adsorption calculations are indicated by circles. Considering the symmetry of the 1/1 AC, adsorption calculations were performed within the square-enclosed region. The positions of surface atoms are also indicated.

However, the influence of rare-earth substitution was smaller than that of Al or Pt substitution. These results indicate that the impact of elemental substitution on catalytic properties strongly depends on the specific crystallographic site being modified. Among all substitutions examined, replacing Ga with Al produced the most pronounced enhancement.

In this study, catalytic rates were normalized by BET surface area because mass-normalized rates can be strongly influenced by particle

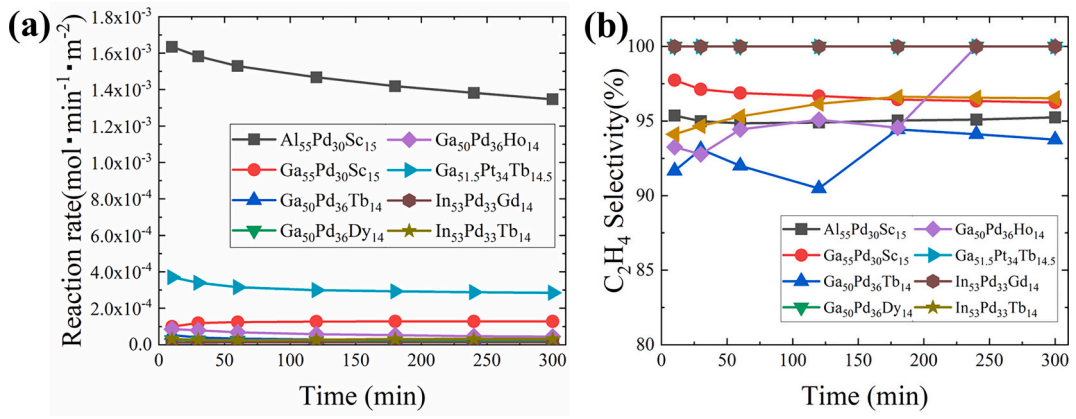


Fig. 4. Catalytic properties of various Tsai-type 1/1 AC samples for C_2H_2 hydrogenation at 200 °C. (a) C_2H_2 reaction rate normalized by surface area. (b) C_2H_4 selectivity.

size, whereas BET surface area better reflects the exposed surface area of the alloy particles. Although the BET surface areas of Tsai-type ACs are relatively low due to their bulk alloy nature, BET normalization still provides a practical basis for comparing catalytic performance. We note, however, that BET-normalized rates do not directly represent intrinsic activity in terms of active-site density. TOF values, or Pd-site-normalized activities were not included because the dominant surface orientations and the number of catalytically active Pd sites have not yet been experimentally determined.

During all catalytic tests, reaction products were continuously monitored using an online GC system equipped with TCD and FID detectors. Only C_2H_2 and C_2H_4 were detected throughout the reaction, and no hydrocarbons associated with C—C coupling or other side reactions were observed under the present reaction conditions. To evaluate catalyst stability, isothermal acetylene hydrogenation was conducted at 200 °C for 5 h. The $Al_{55}Pd_{30}Sc_{15}$ sample exhibited a gradual decrease in reaction rate during the test period. Although these results provide an initial assessment of stability, longer-term and higher-temperature durability tests will be required to fully establish catalyst robustness.

To further clarify the roles of electronic structure and geometric effects, we focused on the Al–Pd–Sc and Ga–Pd–Sc systems for detailed electronic-state analysis and DFT calculations.

3.2. HAXPES analyses

The Pd 3d spectra of Al-Pd-Sc 1/1 AC, Ga-Pd-Sc 1/1 AC, and the Pd metal are shown in Fig. 5. The $3d_{5/2}$ peak of Pd metal appears at 335.0 eV, and the $3d_{3/2}$ peak appears at 340.3 eV. By contrast, the 3d peaks in Al-Pd-Sc and Ga-Pd-Sc were shifted to the high-binding-energy side by 2.0 and 1.6 eV, respectively, compared to that of metallic Pd. The Pauling electronegativities of Al, Ga, and Pd are 1.5, 1.6, and 2.2, respectively [43]. Because the electronegativity difference between Al and Pd is larger than that between Ga and Pd, the larger shift observed for Al–Pd–Sc is consistent with stronger charge transfer from Al to Pd. However, such binding-energy shifts cannot be explained solely by electronegativity differences. As reported for Ni and Pd alloys, the movement of the d-band centroid to higher binding energy is largely driven by hybridization between Pd d states and the bands of partner elements, accompanied by changes in bandwidth and a reduction in the d-state density near the Fermi level [38]. This electronic-structure interpretation complements the compositional dependence observed in Al—Pd binary alloys.

The peak position of Pd $3d_{3/2}$ in Al—Pd binary alloys is reported to be 340.75 eV for $Al_{0.1}Pd_{0.9}$, 342.35 eV for AlPd, and 342.90 eV for Al_3Pd [44], indicating that the Al/Pd ratio in Al—Pd binary alloys significantly affects the Pd 3d spectra. For $Al_{55}Pd_{30}Sc_{15}$, the Al/Pd ratio was 1.83, which lay between the values for AlPd and Al_3Pd. The peak position of

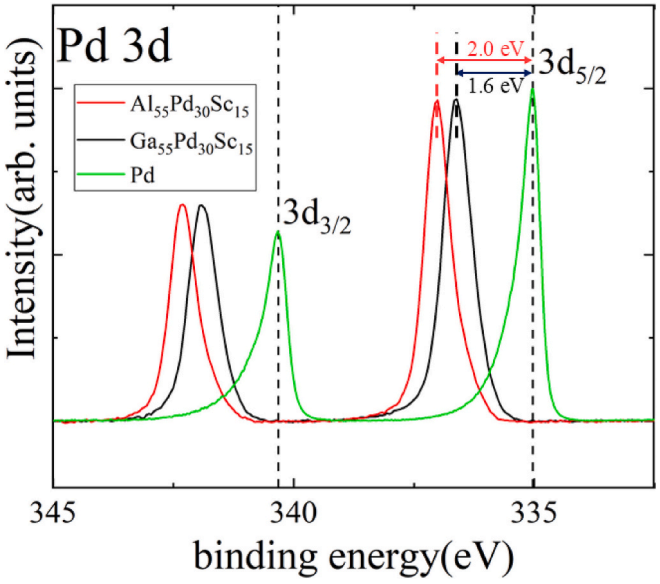


Fig. 5. Pd 3d spectra of Al-Pd-Sc 1/1 AC (red), Ga-Pd-Sc 1/1 AC (black), and Pd (green). (For interpretation of the references to colour in this figure legend, the reader is referred to the web version of this article.)

Pd 3d in Al-Pd-Sc was also between those of AlPd and Al_3Pd, showing that the Al/Pd ratio in the Al-Pd-Sc ternary alloy affected the Pd 3d spectra like that in the Al—Pd binary alloy. For Tsai-type ACs, some systems can be synthesized over a wide compositional range [45]. The experimental results suggested that the chemical shift could be controlled by the composition of the alloy system.

The Al 1 s and Ga $2p_{3/2}$ spectra are shown in Fig. 6. Peak deconvolution using Voigt functions reveals three components for both Al 1 s and Ga $2p_{3/2}$. Peaks at 1561.7 eV (Al 1 s) and 1117.8 eV (Ga $2p_{3/2}$) correspond to native surface oxides [46–48]. Metallic Al contributes peaks at 1559.5 and 1559.3 eV, while metallic Ga appears at 1116.7 eV [47,49]. The splitting of the metallic Al 1 s peak likely arises from the presence of eight nonequivalent crystallographic sites in the 1/1 AC structure, six of which are occupied by Al and four by Pd [14,37]. The observed peak splitting therefore suggests that Al atoms at different nonequivalent sites experience distinct electronic environments. These variations in electronic state are considered to contribute to differences in catalytic activity among the nonequivalent sites.

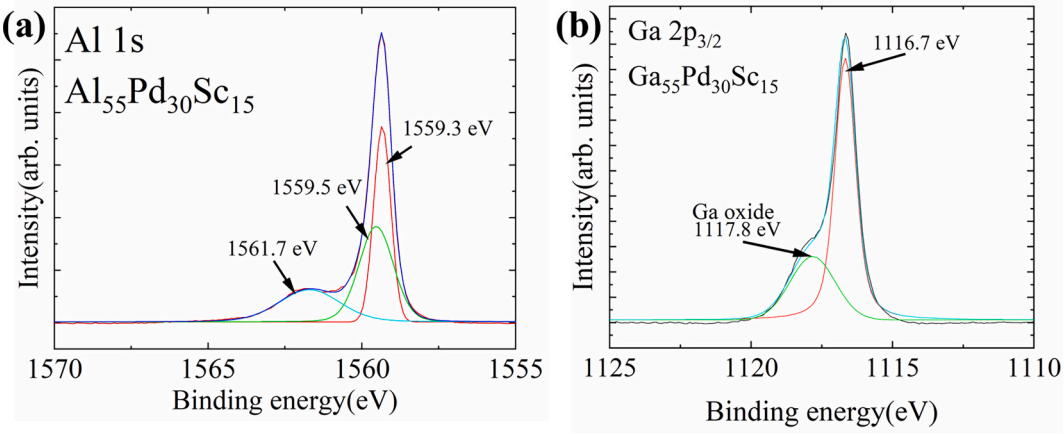


Fig. 6. (a) Al 1 s (b) Ga $2p_{3/2}$ spectra. The Voight function was used to deconvolute the peaks. Three peaks, including an oxide component, appear in the Al 1 s spectrum, while two peaks appear in the Ga $2p_{3/2}$ spectrum.

3.3. DFT calculations

3.3.1. Adsorption energies of C_2H_2, C_2H_3, and C_2H_4

Fig. 7 shows the adsorption energies of C_2H_2, C_2H_3, and C_2H_4 at different sites on Al-Pd-Sc (Figs. 7(a), (c), and (e)) and Ga-Pd-Sc (Figs. 7 (b), (d), and (f)), where the magnitude of the adsorption energy at each site is represented by the colour in the corresponding colour scale shown. The detailed results of the calculated adsorption energies are listed in Table S1. The adsorption energies of C_2H_2 and C_2H_3 on the Al-Pd-Sc surface were lower than those on the corresponding sites of Ga-Pd-Sc, whereas the adsorption energy of C_2H_4 showed the opposite trend. This indicates that C_2H_2 and C_2H_3 preferentially adsorb on Al-Pd-Sc, while C_2H_4 is more stable on Ga-Pd-Sc. As shown in Fig. 7, for both Al-Pd-Sc and Ga-Pd-Sc, the adsorption energy of C_2H_2 tends to be lower when the initial adsorption site is near the Sc atom, except for a few sites (such as site 5 in Fig. 7(a)) near Al. The relaxed adsorption structures are shown in Fig. S3. The positions with relatively low adsorption energies for C_2H_2 on Al-Pd-Sc were classified into four types: (1) hollow sites consisting of Al, Pd, and Sc (M1-M2-Sc site), (2) hollow sites consisting of two Pd and one Sc, (3) hollow sites consisting of three Al (M1-M4-M4 site), and (4) bridge sites consisting of Al and Sc. Here, M1 and M4 are Al-occupied sites, and M2 and M5 are Pd-occupied sites. On Ga-Pd-Sc, two types of positions with relatively low adsorption energies for C_2H_2 were identified: (1) hollow sites consisting of Ga, Pd, and Sc (M1-M2-Sc site), and (2) hollow sites consisting of two Pd and one Sc (M2-M5-Sc site). In contrast, the adsorption energy of C_2H_3 was lower only at the M1-M2-Sc site. However, the adsorption position of C_2H_4 was found to be at the Sc-top site in both Al-Pd-Sc and Ga-Pd-Sc, and additionally at the M1-M2-Sc site in Al-Pd-Sc. These results suggest that C_2H_2 adsorbed at the M1-M2-Sc site on Al-Pd-Sc can be hydrogenated to C_2H_4 without requiring long-distance diffusion. In Ga-Pd-Sc, however, C_2H_2 adsorbed at the M1-M2-Sc site likely diffuses to the Sc-top site to form C_2H_4 before hydrogenation, which may introduce an additional kinetic barrier for the reaction.

We emphasize that the identification of active sites in this study is based solely on DFT adsorption-energy calculations. Although these results provide insight into the most reactive crystallographic positions, determining the exact active sites and elemental occupation on real catalyst surfaces under reaction conditions remains experimentally challenging. Further experimental verification will be required to confirm these theoretical predictions.

3.3.2. Analysis of the reaction mechanisms using NEB calculations

Based on the adsorption energies and relaxed structures, NEB calculations were performed using adsorption configurations of C_2H_2, C_2H_3, or C_2H_4 at the M1-M2-Sc site as initial and final states. For Al-Pd-Sc, additionally calculations were conducted using the M1-M4-M4 site as the initial and final states, which exhibited the lowest C_2H_2 adsorption energy. The adsorption site of H atoms was determined by evaluating H adsorption energies at neighboring positions.

C_2H_2 hydrogenation (Eq. (1)) is proposed to comprise the following elementary reactions (Eqs. (2)–(6)) [50].

$$C_2H_2 + H_2 \rightarrow C_2H_4 \quad (1)$$

$$C_2H_2 + {}^* \rightarrow C_2H_2{}^* \quad (2)$$

$$H_2 + 2{}^* \rightarrow 2H{}^* \quad (3)$$

$$C_2H_2{}^* + H{}^* \rightarrow CHCH_2{}^* \quad (4)$$

$$CHCH_2{}^* + H{}^* \rightarrow C_2H_4{}^* + {}^* \quad (5)$$

$$C_2H_4{}^* \rightarrow C_2H_4 + {}^* \quad (6)$$

C_2H_2 adsorbs on the metal surface owing to the bonding of the π-electrons that form the triple bonds between two carbon atoms, with the d-electrons of the metal surface (Eq. (2)), while H_2 dissociatively adsorbs on the surface to form H atoms (Eq. (3)). These H atoms subsequently react with C_2H_2 (Eq. (4)), and C_2H_3 (Eq. (5)) to form C_2H_4. Because only a small amount of C_2H_6 was detected experimentally, further hydrogenation of C_2H_4 was not considered in the NEB calculations.

Fig. 8 shows the calculated activation energy barrier for the elementary reactions at the M1-M2-Sc site of Al-Pd-Sc (Figs. 8(a) and (b)) and Ga-Pd-Sc (Figs. 8(e)) and (f)), and at the M1-M4-M4 site of Al-Pd-Sc (Figs. 8(c) and (d)), with the corresponding structures of the initial and final states, including the H atom. For Al-Pd-Sc, the activation energies at the M1-M2-Sc site are 22.5 kJ/mol for C_2H_3 formation (Eq. (4)) and 67.2 kJ/mol for C_2H_4 formation (Eq. (5)). These values are significantly lower than those at the M1-M4-M4 site (117.8 kJ/mol for C_2H_3 formation and 86.0 kJ/mol for C_2H_4 formation). Similar to the adsorption energy results, these results suggest that the M1-M2-Sc site functions as an active site on Al-Pd-Sc. The rate-determining step in the reaction at this site is the hydrogenation of C_2H_3 (Eq. (5)) (Figs. 8(a) and (b)).

For Ga-Pd-Sc, the activation energies at the M1-M2-Sc site are 14.6 kJ/mol for C_2H_3 formation and 77.4 kJ/mol for C_2H_4 formation (Figs. 8 (e) and (f)), suggesting that the rate-determining step is the same as that on Al-Pd-Sc. The activation barrier for C_2H_3 hydrogenation of Al-Pd-Sc is 10.2 kJ/mol smaller than that of Ga-Pd-Sc, which is consistent with our previous experimental results in which the difference between the apparent activation energies of the Al-Pd-Sc and Ga-Pd-Sc catalysts was

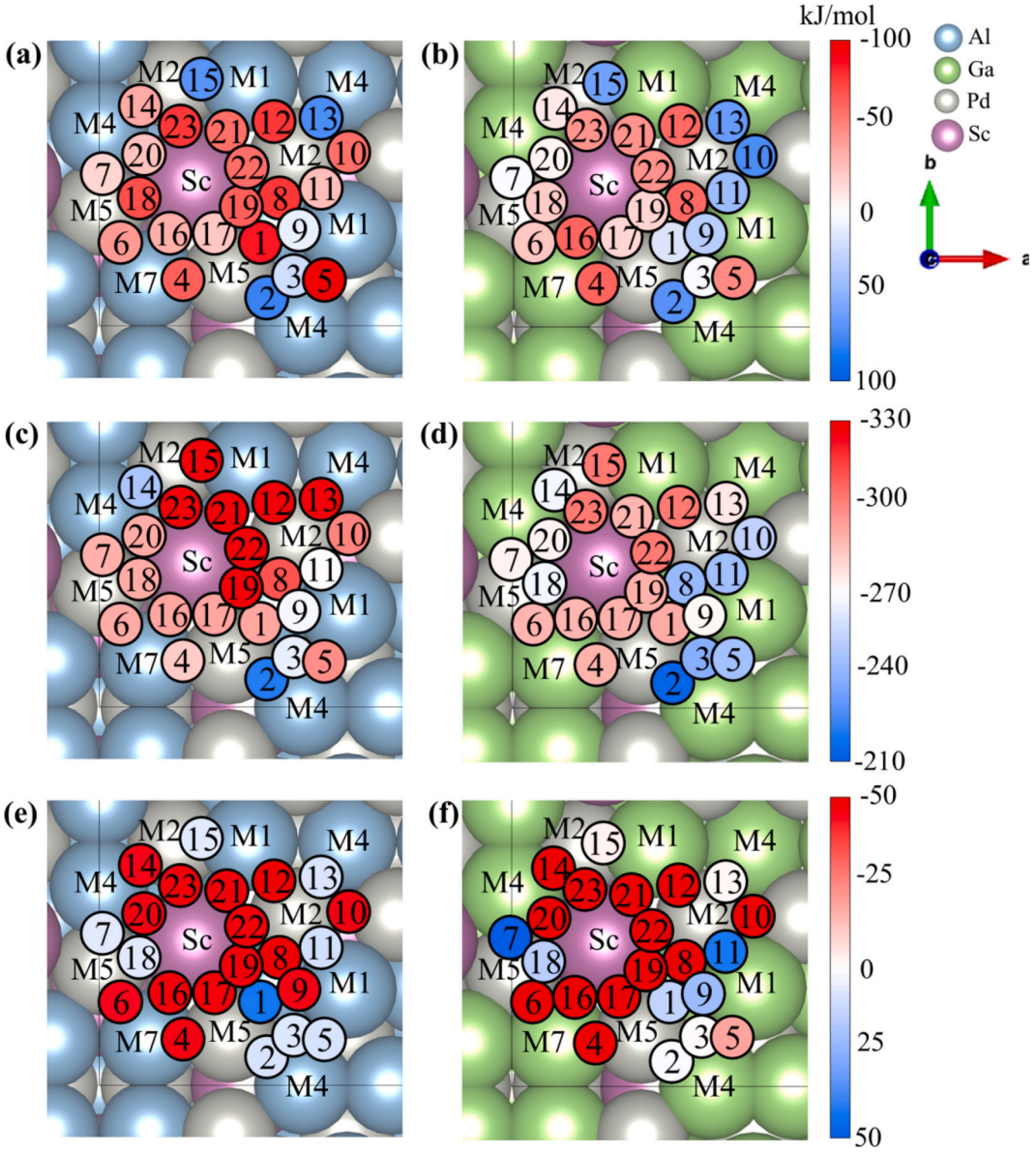


Fig. 7. Adsorption energy for each initial state. (a) C_2H_2 on the Al-Pd-Sc surface. (b) C_2H_2 on the Ga-Pd-Sc surface. (c) C_2H_3 on the Al-Pd-Sc surface. (d) C_2H_3 on the Ga-Pd-Sc surface. (e) C_2H_4 on the Al-Pd-Sc surface. (f) C_2H_4 on the Ga-Pd-Sc surface. Sites with low adsorption energy are shown in red, whereas sites with high adsorption energy are shown in blue. The crystallographic positions of surface atoms are indicated in the figure. (For interpretation of the references to colour in this figure legend, the reader is referred to the web version of this article.)

12.1 kJ/mol [36]. These results confirm that the M1-M2-Sc sites serve as the active site for C_2H_2 hydrogenation and that the differences in activation energy at these sites in Al-Pd-Sc and Ga-Pd-Sc 1/1 ACs account for the observed catalytic performance differences.

Furthermore, we performed differential charge-density calculations for the adsorption of C_2H_2, C_2H_3, and C_2H_4 on the M1–M2–Sc site of Al–Pd–Sc. The resulting charge-density difference maps (Figs. S4–S6) show regions of increased electron density in yellow. These results indicate that adsorbed C_2H_2, C_2H_3, and C_2H_4 interact not only with the Sc and Pd atoms directly beneath the adsorbate but also exhibit spatial electronic overlap with adjacent Al atoms. Consequently, the adsorbates do not bind vertically to a single atom; instead, they stabilize in a hollow-site configuration through multicenter bonding involving Sc, Pd, and nearby Al atoms. This behavior is consistent with the strong hybridization effects discussed in the HAXPES analyses.

To evaluate the role of hydrogen activation in the acetylene hydrogenation process, we additionally calculated the adsorption energies of both hydrogen molecules and hydrogen atoms at various surface sites of the Al–Pd–Sc slab model. The adsorption energies of H_2 were found to range from −0.3 to 5.4 kJ/mol, whereas atomic hydrogen exhibited much stronger adsorption, with values between −355.0 and − 295.0 kJ/mol (Table S2).

CI-NEB calculations were performed using the adsorbed H_2 configuration with the lowest adsorption energy (site 4 in Table S2) as the initial state and several neighboring H-stabilizing sites as final states. The resulting H_2 dissociation barriers fall within 25.3–36.6 kJ/mol (Fig. S7), indicating that hydrogen activation is energetically feasible under the reaction conditions. These results support the proposed reaction mechanism and confirm that hydrogen activation does not limit the overall acetylene hydrogenation process on Tsai-type 1/1 AC surfaces.

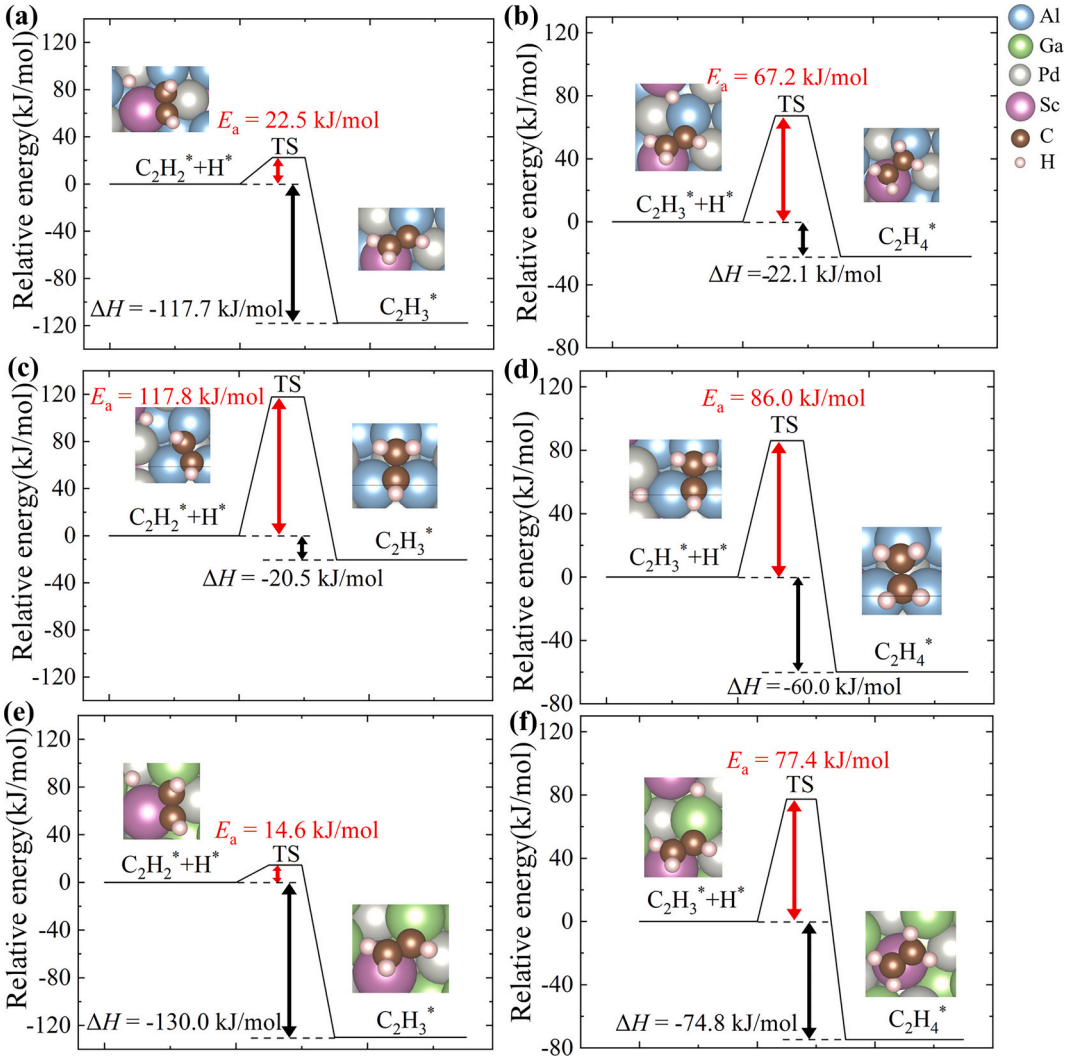


Fig. 8. Relative energy of the transition state (TS) and enthalpy change (ΔH) during the reaction, calculated using the climbing image nudged elastic band (CI-NEB) method. The energy of the initial state of each elementary reaction is taken as the reference (zero). Activation energies (E_a) are marked with red arrows, and ΔH values are marked with black arrows. (a) C_2H_3 formation on the M1-M2-Sc site of Al-Pd-Sc. (b) C_2H_4 formation on the M1-M2-Sc site of Al-Pd-Sc. (c) C_2H_3 formation on the M1-M4-M4 site of Al-Pd-Sc. (d) C_2H_4 formation on the M1-M4-M4 site of Al-Pd-Sc. (e) C_2H_3 formation on the M1-M2-Sc site of Ga-Pd-Sc. (f) C_2H_4 formation on the M1-M2-Sc site of Ga-Pd-Sc. (For interpretation of the references to colour in this figure legend, the reader is referred to the web version of this article.)

4. Conclusions

The effects of elemental substitution on acetylene hydrogenation in Tsai-type 1/1 ACs, (Al, Ga, In)-(Pd, Pt)-(Sc, Tb, Dy, Ho), were systematically investigated. Among all substitutions examined, replacing Ga or In with Al produced the strongest enhancement in catalytic activity, followed by substituting Pt for Pd, whereas substitution among rare-earth elements had only a minor influence. The Al–Pd–Sc system exhibited the highest catalytic activity among the tested compositions. HAXPES measurements revealed that the Pd 3d binding energy in Al-Pd-Sc shifted to higher values compared with Ga–Pd–Sc, despite their similar geometric structures. This indicates that the electronic state of Pd—the active metal for acetylene hydrogenation—can be effectively tuned through elemental substitution, particularly by replacing Ga(In) with Al. DFT calculations revealed that the adsorption energies of C_2H_2, C_2H_3, and C_2H_4 vary significantly with elemental substitutions and differ among nonequivalent crystallographic sites within the same Al-Pd-Sc(100) or Ga-Pd-Sc(100). C_2H_2 was found to be more easily adsorbed on the Al-Pd-Sc surface, and smaller energy barriers were required for C_2H_2 hydrogenation than on the Ga-Pd-Sc surface. These findings suggest the possibility of designing catalysts based on precise control of both the electronic state and geometric structure using the characteristics of QC/ACs.

CRediT authorship contribution statement

Haruka Yoshikawa: Writing – original draft, Investigation. **Ya Xu:** Writing – review & editing, Supervision. **Farid Labib:** Investigation. **Satoshi Kameoka:** Investigation. **Ryuji Tamura:** Supervision.

Funding

This work was supported by Grants-in-Aid for Scientific Research (Grants No. JP19H05817, JP19H05818, JP22H01804, JP23K23072) from the Japan Society for the Promotion of Science, a Strategic Basic Research Program CREST (Grant No. JPMJCR22O3) from the Japan Science and Technology Agency (JST), Japan.

Declaration of competing interest

The authors declare that they have no known competing financial interests or personal relationships that could have appeared to influence

the work reported in this paper.

Acknowledgements

The calculations in this study were performed on the Numerical Materials Simulator at NIMS. The HAXPES measurements were performed at BL09XU beam line of Spring-8 (Proposal no. 2023A1037, 2023B1042, 2023B1935, 2024A1669, 2024B1581). H. Yoshikawa appreciates the support of the Material Science Human Resource Development Fellowship of Tokyo University of Science.

Appendix A. Supplementary data

Supplementary data to this article can be found online at https://doi.org/10.1016/j.apcato.2026.207117.

Data availability

Data will be made available on request.

References

[1] K. Tarama, Phisico-Chemical Theory of Catalysis, Chijinsyhokan & Co., Ltd, Tokyo, 1966, pp. 95-116, 118.
[2] K. Eguchi, Catalytic Chemistry, Maruzen Publishing, Tokyo, 2011.
[3] C. Guo, X. Zhang, L.G. Wang, Y.X. Tang, H. Wang, T.T. Zhao, S.K. Xiao, Z.Y. Yang, B.W. Zhou, Y.Y. Jiang, F.L. Wang, Densely-neighbored-Ru nanoparticles confined in porous-SiO2 shell for efficient CO2 methanation via plasmon-coupling-enhanced photo-thermal catalysis, Sci. Bull. 70 (2025) 3534–3543.
[4] Y.X. Tang, H. Wang, C. Guo, Z.Y. Yang, T.T. Zhao, J.R. Liu, Y.Y. Jiang, W.L. Wang, Q. Zhang, D.S. Wu, Y.F. Zhao, X.D. Wen, F.L. Wang, Ruthenium-cobalt solid-solution alloy nanoparticles for enhanced photopromoted thermocatalytic CO hydrogenation to methane, ACS Nano 18 (2024) 11449–11461.
[5] Y.X. Tang, H. Wang, C. Guo, L.G. Wang, T.T. Zhao, S.K. Xiao, J.R. Liu, Y.Y. Jiang, Y. F. Zhao, X.D. Wen, F.L. Wang, Synergies between atomically dispersed Ru single atoms and nanoparticles on CeAlOx for enhanced photo-thermal catalytic CO2 hydrogenation, Adv. Mater. 38 (2026).
[6] B. Lambert, W. Hume-Rothery, Studies of precipitated solids. Part I. Strontium sulphate, J. Chem. Soc. (1926) 2637–2648.
[7] N. Sato, T. Ishimasa, Science of Quasicrystals, The University Nagoya Press, Aichi, 2024, pp. 168–195.
[8] S. Takeuchi, K. Edagawa, A.P. Tsai, K. Kimura, Phisics of Quasicrystals, Asakura Publishing Co., Ltd., Tokyo, 2012.
[9] A.P. Tsai, A test of Hume-Rothery rules for stable quasicrystals, J. Non-Cryst. Solids 334 (2004) 317–322.
[10] Y.G. So, K. Takagi, T.J. Sato, Effects of Pt substitution on the formation and magnetic behavior of a Ga-Pd-Tb 2/1 approximant, 10th international conference on aperiodic crystals, Aperiodic 2022, 2461, 2023.
[11] T. Fukushima, R. Tsukuda, S. Ohhashi, N. Fujita, S. Kameoka, One-step synthesis of non-equilibrium Pd-Ru alloys from Al-Pd-Ru quasicrystals and approximants, in: 10th International Conference on Aperiodic Crystals, Aperiodic 2022 2461, 2023.
[12] F. Labib, H. Takakura, A. Ishikawa, R. Tamura, Competition between spin-glass and antiferromagnetic states in Tsai-type 1/1 and 2/1 quasicrystal approximants, Phys. Rev. Mater. 6 (2022).
[13] F. Labib, N. Fujita, S. Ohhashi, A.P. Tsai, Icosahedral quasicrystals and their cubic approximants in the cd-Mg-RE (RE = Y, Sm, Gd, Tb, Dy, ho, Er, tm) systems, J. Alloys Compd. 822 (2020).
[14] Y.G. So, A. Katagiri, R. Tamura, K. Edagawa, Formation of Ga-Pd-Sc icosahedral quasicrystal and approximant phases, Philos. Mag. Lett. 98 (2018) 292–300.
[15] Y.G. So, F. Saruhashi, K. Kimoto, R. Tamura, K. Edagawa, Formation of Tsai-type 1/1 approximants in in-Pd-RE (RE: rare earth metal) alloys, Philos. Mag. 94 (2014) 2980–2991.
[16] Y.G. So, T. Yoshikawa, F. Saruhashi, K. Edagawa, R. Tamura, Formation of icosahedral quasicrystals and 1/1 crystal approximants in Al-Pd-RE (RE: rare earth metals) systems, Mater. Trans. 52 (2011) 2011–2015.
[17] Y. Morita, A.P. Tsai, Approximants in the ag-in-M and au-Sn-M (M = ca or rare earth metals) systems, Jpn. J. Appl. Phys. 47 (2008) 7975–7979.
[18] A.P. Tsai, Formation of quasicrystals and Hume-Rothery rules, J. Crystallogr. Soc. Jpn. 49 (2007) 12–17.
[19] A. Yamamoto, H. Takakura, A.P. Tsai, Six-dimensional model of icosahedral Al-Pd-Mn quasicrystals, Phys. Rev. B 68 (2003).
[20] J.Q. Guo, A.P. Tsai, Stable icosahedral quasicrystals in the Ag-In-Ca, Ag-In-Yb, Ag-In-Ca-Mg and Ag-In-Yb-Mg systems, Philos. Mag. Lett. 82 (2002) 349–352.
[21] J.Q. Guo, E. Abe, A.P. Tsai, Stable cd-Mg-Yb and cd-Mg-ca icosahedral quasicrystals with wide composition ranges, Philos. Mag. Lett. 82 (2002) 27–35.
[22] A.P. Tsai, J.Q. Guo, E. Abe, H. Takakura, T.J. Sato, Alloys - a stable binary quasicrystal, Nature 408 (2000) 537–538.
[23] A.P. Tsai, A. Inoue, Y. Yokoyama, T. Masumoto, Stable icosahedral Al-Pd-Mn and Al-Pd-re alloys, Mater. T Jim. 31 (1990) 98–103.
[24] T. Ishimasa, Y. Kaneko, H. Kaneko, New group of stable icosahedral quasicrystals: structural properties and formation conditions, J. Non-Cryst. Solids 334 (2004) 1–7.
[25] S. Suzuki, A. Ishikawa, T. Yamada, T. Sugimoto, A. Sakurai, R. Tamura, Magnetism of Tsai-type quasicrystal approximants, Mater. Trans. 62 (2021) 298–306.
[26] T. Tanabe, S. Kameoka, A.P. Tsai, A novel catalyst fabricated from Al-cu-Fe quasicrystal for steam reforming of methanol, Catal. Today 111 (2006) 153–157.
[27] A.P. Tsai, M. Yoshimura, Highly active quasicrystalline Al-cu-Fe catalyst for steam reforming of methanol, Appl. Catal. A-Gen. 214 (2001) 237–241.
[28] A. Zieba, K. Stan-Glowinska, D. Duraczynska, M. Marzec, A. Góral, P. Czaja, L. Rogal, L. Litynska-Dobrzynska, Al-Ni-co decagonal quasicrystal application as an energy-effective catalyst for phenylacetylene hydrogenation, Sustain. Mater. Technol. 41 (2024).
[29] M. Yoshimura, A.P. Tsai, Quasicrystal application on catalyst, J. Alloys Compd. 342 (2002) 451–454.
[30] M. Krajcí, J. Hafner, Catalytic properties of Al13Co4 studied by ab initio methods, Philos. Mag. 91 (2011) 2904–2912.
[31] D. Kandaskalov, V. Fournée, J. Ledieu, E. Gaudry, Catalytic Semihydrogenation of acetylene on the (100) surface of the o-Al13Co4 Quasicrystalline approximant: density functional theory study, J. Phys. Chem. C 121 (2017) 18738–18745.
[32] K. Abe, R. Tsukuda, N. Fujita, S. Kameoka, High catalytic performance of Al-Pd-(Ru, Fe) icosahedral approximants for acetylene semi-hydrogenation, RSC Adv. 11 (2021) 15296–15300.
[33] Z. Almisbaa, H.A. Aljama, K. Almajnouni, L. Cavallo, P. Sautet, Acetylene semi-hydrogenation on intermetallic Ni-in catalysts: Ni ensemble and acetylene coverage effects from a theoretical analysis, ACS Catal. 13 (2023) 7358–7370.
[34] D. Albani, M. Capdevila-Cortada, G. Vilé, S. Mitchell, O. Martin, N. López, J. Pérez-Ramírez, Semihydrogenation of acetylene on indium oxide: proposed single-ensemble catalysis, Angew. Chem. Int. Edit. 56 (2017) 10755–10760.
[35] G. Tiwari, S. Sarkar, B.R. Jagirdar, Bimetallic catalysts in acetylene semi-hydrogenation: conceptual advances and challenges, Chemcatchem 16 (2024).
[36] H. Yoshikawa, F. Labib, Y. Xu, R. Tamura, Catalytic properties and their relation with adsorption energies calculated by density functional theory in Pd-containing 1/1 approximant crystals, Mater. Trans. 64 (2023) 2425–2430.
[37] Y.G. So, M. Nagao, T. Nagai, K. Kimoto, HAADF-STEM study of chemical ordering in Al-Pd-Sc 1/1-crystal approximant, J. Alloys Compd. 543 (2012) 7–11.
[38] J.C. Fuggle, F.U. Hillebrecht, R. Zeller, Z. Zolnierek, P.A. Bennett, C. Freiburg, Electronic-structure of Ni and Pd alloys .1. X-ray photoelectron-spectroscopy of the valence bands, Phys. Rev. B 27 (1983) 2145–2178.
[39] Y.G. So, K. Edagawa, Formation of icosahedral quasicrystal and its 1/1 crystal approximant in Al-Pd-Sc system, Mater. Trans. 50 (2009) 948–951.
[40] Y.G. So, K. Takagi, T.J. Sato, Formation and magnetic properties of Ga-Pd-Tb 2/1 approximant, J. Phys. Conf. Ser. 1458 (2020).
[41] T. Yamasaki, A. Kuroda, T. Kato, J. Nara, J. Koga, T. Uda, K. Minami, T. Ohno, Multi-axis decomposition of density functional program for strong scaling up to 82,944 nodes on the K computer: compactly folded 3D-FFT communicators in the 6D torus network, Comput. Phys. Commun. 244 (2019) 264–276.
[42] S. Coates, K. Nozawa, M. Fukami, K. Inagaki, M. Shimoda, R. McGrath, H. R. Sharma, R. Tamura, Atomic structure of the (111) surface of the antiferromagnetic 1/1 au-Al-Tb approximant, Phys. Rev. B 102 (2020).
[43] L. Pauling, The Nature of the Chemical Bond, Cornell University, 1960, p. 93.
[44] F.U. Hillebrecht, J.C. Fuggle, P.A. Bennett, Z. Zolnierek, C. Freiburg, Electronic-structure of Ni and Pd alloys .2. X-ray photoelectron core-level spectra, Phys. Rev. B 27 (1983) 2179–2193.
[45] A. Ishikawa, T. Hiroto, K. Tokiwa, T. Fujii, R. Tamura, Composition-driven spin glass to ferromagnetic transition in the quasicrystal approximant au-Al-Gd, Phys. Rev. B 93 (2016).
[46] A. Beni, N. Ott, M. Pawelkiewicz, M. Wardé, K. Young, B. Bauer, P. Rajput, B. Detlefs, J. Zegenhagen, R. McGrath, M.G. Barthés-Labrousse, L.P.H. Jeurgens, P. Schmutz, Hard X-ray photoelectron spectroscopy (HAXPES) characterisation of electrochemical passivation oxide layers on Al-Cr-Fe complex metallic alloys (CMAs), Electrochem. Commun. 46 (2014) 13–17.
[47] J.F.B. Moulder, W.F. Stickle, P.E. Sobol, K.D. Bomben, Handbook of X-Ray Photoelectron Spectroscopy, ULVAC-PHI, Kanagawa, 1995.
[48] Y. Xu, H. Yoshikawa, J.H. Jang, M. Demura, K. Kobayashi, S. Ueda, Y. Yamashita, D.M. Wee, T. Hirano, Characterization of surface structure evolution in Ni3Al foil catalysts by hard X-ray photoelectron spectroscopy, J. Phys. Chem. C 114 (2010) 6047–6053.
[49] S. Yasuno, T. Matsumoto, H. Nagao, H. Yoshikawa, MDR HAXPES DB, Materials Data Repository, 2021.
[50] G.C. Bond, P.B. Wells, Hydrogenation of acetylene .1. Reaction of acetylene with hydrogen catalyzed by alumina-supported platinum, J. Catal. 4 (1965) 211–219.